Science Advances

AAAS

advances.sciencemag.org/cgi/content/full/3/7/e1700225/DC1

Supplementary Materials for

Dual-color single-mode lasing in axially coupled organic nanowire resonators

Chunhuan Zhang, Chang-Ling Zou, Haiyun Dong, Yongli Yan, Jiannian Yao, Yong Sheng Zhao

Published 14 July 2017, *Sci. Adv.* **3**, e1700225 (2017)
DOI: 10.1126/sciadv.1700225

This PDF file includes:

- section S1. Synthesis procedure and luminescence properties of the model compounds
- section S2. Structural characterizations and lasing measurements of the isolated OPV-A and OPV-B NWs
- section S3. Construction of the axially coupled heterogeneous NW resonators with effective mode modulation
- section S4. Numerical simulation of the effective refractivity and threshold gain
- fig. S1. The synthetic route of compound OPV-A.
- fig. S2. The synthetic route of compound OPV-B.
- fig. S3. Normalized fluorescence spectra of the OPV-A and OPV-B powders.
- fig. S4. Absolute fluorescence quantum yields (Φ) of OPV-A and OPV-B powders.
- fig. S5. XRD patterns of OPV-A and OPV-B NWs and powder samples.
- fig. S6. Optical waveguiding properties of OPV-A and OPV-B NWs.
- fig. S7. Schematic illustration of the homebuilt setup for optical characterization.
- fig. S8. Microcavity effects of uncoupled NWs.
- fig. S9. Schematic diagram of the fabrication process of the axially coupled heterogeneous NWs.
- fig. S10. Controllable fabrication of the axially coupled heterogeneous NW cavities.
- fig. S11. Three-dimensional numerical simulation of the output field from the NW end facet.
- fig. S12. Influence of gap distance on the mode modulation.
- fig. S13. Schematic diagram of the construction strategy of the desired gap distance for axially coupled heterogeneous NW resonators.

- fig. S14. Coupling effect of axially coupled heterogeneous NW cavities.
- fig. S15. Evolution of the emission spectra with the increase of pump power for isolated and heterogeneously coupled NWs.
- fig. S16. Lasing characterization of the OPV-B NW coupled with OPV-A NWs of different lengths.
- fig. S17. Lasing characterization of the axially coupled heterogeneous NWs with varying gap distances.
- fig. S18. Theory model.
- References (*54–58*)

section S1. Synthesis procedure and luminescence properties of the model compounds

The model compounds were synthesized with Knoevenagel condensation reactions (fig. S1 and S2). Figure S3 shows the normalized fluorescence spectra of the OPV-A and OPV-B powders with the maximum emission at ~460 and ~560 nm, respectively. The solid-state fluorescence quantum yields of these two compounds are of 69.6% and 47.9%, respectively (fig. S4).

Materials:

1,4-Dibromo-2,5-dimethylbenzene,4-(diphenylamino)benzaldehyde, potassium tertobutoxide, and tetra-butyl ammonium hydroxide were purchased from Aldrich. 2,5-Dibromobenzene-1,4-dicarbaldehydewas purchased from InnoChem Science & Technology (Beijing, China). All compounds were used without further treatment.

Synthesis of Cyano-substituted oligo(*p*-phenylenevinylene) (OPV-A)

Step 1: Synthesis of [1,1';4',1''] terphenyl-2',5'-dicarbaldehyde (*54*)

A mixture of 2,5-dibromobenzene-1,4-dicarbaldehyde (1.0 g), phenylboronic acid (1.1 g), $Pd(PPh_3)_4$ (0.2 g), toluene (12.5 mL) and 2 M Na_2CO_3 solution (2.5 mL) was refluxed at 85 °C for 36 hours under nitrogen, then poured into water and extracted using dichloromethane. The organic layer was washed with brine and water and dried over $MgSO_4$. The crude product was first purified by flash column chromatography (dichloromethane as eluent) and then recrystallized form chloroform in yield of 81%.

Step 2: Synthesis of OPV-A (*34*)

[1,1';4',1''] terphenyl-2',5'-dicarbaldehyde (0.3 mmol) and phenylacetonitrile (0.6 mmol) were dissolved in tert-butanol (2 mL) and THF (1 mL) at 40 °C under a nitrogen atmosphere. Potassium tert-butoxide (0.05 mmol) and tetra-n-butylammonium hydroxide (0.05mmol, 1 M solution in methanol) were added quickly; then, the mixture was stirred vigorously at 50 °C. After 20 min, the mixture was poured into acidified methanol. The precipitate was collected and dissolved in chloroform and then reprecipitated in methanol. The crude product was purified by column chromatography (silica gel, dichloromethane) in darkness to give the green solid with 70% yield

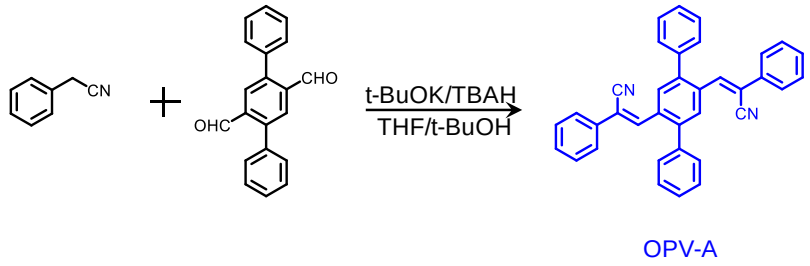

fig. S1. The synthetic route of compound OPV-A.

Synthesis of cyano-substituted oligo-(*α*-phenylenevinylene)-1,4-bis(*R*-cyano-4-diphenylaminostyryl)-2,5-diphenylbenzene (OPV-B)

Step1: Synthesis of 2-(cyanomethyl)-4-(diphenylamino)benzene (*55*)

2-(Cyanomethyl)-4-(diphenylamino)benzene was prepared from 4-(diphenylamino)benzaldehyde upon treatment with tosylmethylisocyanide (TosMIC) and t-BuOK in one single step.

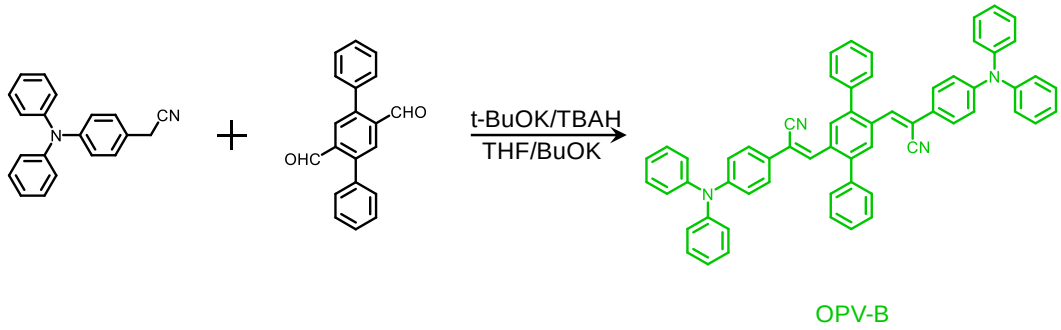

fig. S2. The synthetic route of compound OPV-B.

Step 2: Synthesis of OPV-B (*35*)

2-(Cyanomethyl)-4-(diphenylamino)benzene (0.21 mmol) and [1,1';4',1''] terphenyl-2',5'-dicarbaldehyde (0.1 mmol) were dissolved in tert-butanol (1.2 mL) and THF (0.8 mL) under a nitrogen atmosphere. Potassium tert-butoxide (0.02 mmol) and tetra-n-

butylammonium hydroxide (0.02 mmol, 1 M solution in methanol) were added quickly; then, the mixture was stirred vigorously at 50 °C. After 20 min, the mixture was poured into acidified methanol. The crude product was precipitated from methanol and further purified by column chromatography under rigorous exclusion of light.

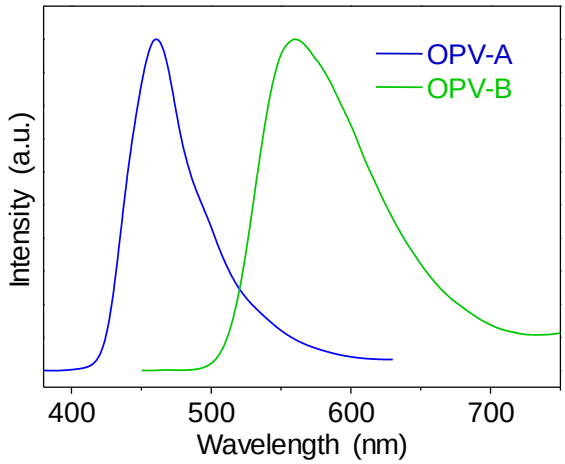

fig. S3. Normalized fluorescence spectra of the OPV-A and OPV-B powders. The OPV-A and OPV-B powders exhibit completely different emission colors, with the maximum emission at ~460 and ~560 nm, respectively. The large difference in wavelength enables the separate study of the lasing characteristics of the two distinct OPV materials.

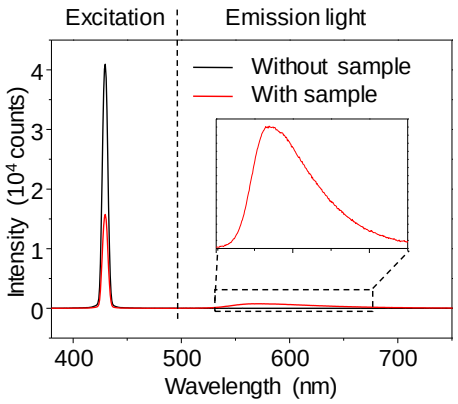

$$\Phi = \frac{A_{em}}{A_{ex,\ without\ sample} - A_{ex,\ with\ sample}}$$

Sample	Quantum yield (Φ)
OPV-A Powders	69.6%
OPV-B Powders	47.9%

fig. S4. Absolute fluorescence quantum yields (Φ) of OPV-A and OPV-B powders.

A_{em} is the integrated intensity of the emission spectra of the sample. $A_{ex,\ with\ sample}$ and $A_{ex,without\ sample}$ are the integrated intensity of the excitation light source with and without sample, respectively.

Quantum yield measurements were performed using the absolute method on a C11347 from Hamamatsu equipped with an integrating sphere, a L11562 Xenon lamp and a CCD detector. The samples of OPV-A and OPV-B powders were measured at an excitation wavelength of 348 nm and 430 nm, respectively. The absolute quantum yields were calculated by comparing the integral of emission and the absorption of excitation light. The OPV-A and OPV-B powders are highly emissive, with very high solid-state fluorescence quantum yield of 69.6% and 47.9%, respectively, which is essential for the optical gain and amplification.

section S2. Structural characterizations and lasing measurements of the isolated OPV-A and OPV-B NWs

Figure S5 displays the X-ray diffraction (XRD) patterns of the OPV-A and OPV-B NWs. The optical waveguiding properties of the OPV-A and OPV-B nanowire are shown in fig. S6. Figure S7 schematically shows the experimental setup for the optical characterization. Figure S8 summarizes the modulated PL spectra of isolated OPV-A and OPV-B NWs with different lengths.

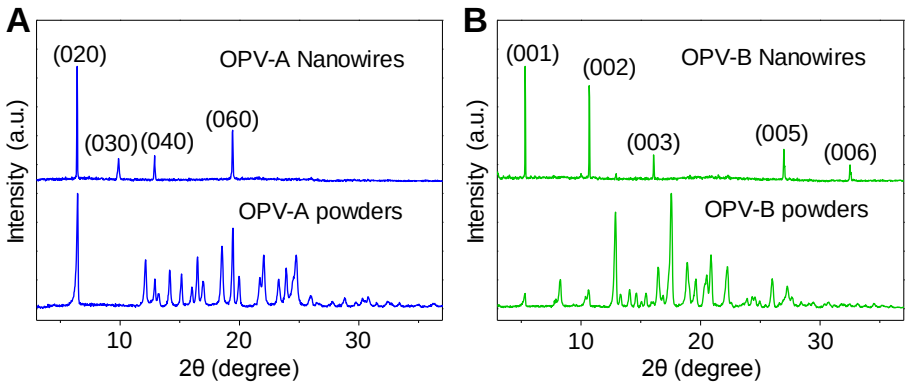

fig. S5. XRD patterns of OPV-A and OPV-B NWs and powder samples. (**A**, **B**) XRD patterns of OPV-A and OPV-B NWs and powder samples.

The diffraction peaks in the X-ray diffraction (XRD) patterns of the OPV-A and OPV-B NWs can be indexed to a monoclinic single crystal (space group: $P\ 2_1/n$, a = 6.645(13), b = 27.561(6), c = 7.6528(15), α = 90°, β = 110.83(3)°, γ = 90°. CCDC No.: 616163) and a triclinic single crystal (space group: P-1, a = 6.6429(13), b = 10.541(2), c = 16.573(3), α = 83.88(3)°, β = 86.20(3)°, γ = 84.05(3)°. CCDC No.: 648728), respectively. This reveals that the OPV-A and OPV-B NWs are highly crystalline structures. The single-crystal nanostructures would exhibit excellent optical properties with very few defects in the material and facilitate optical waveguiding and confinement, which is beneficial for the realization of lasing oscillation.

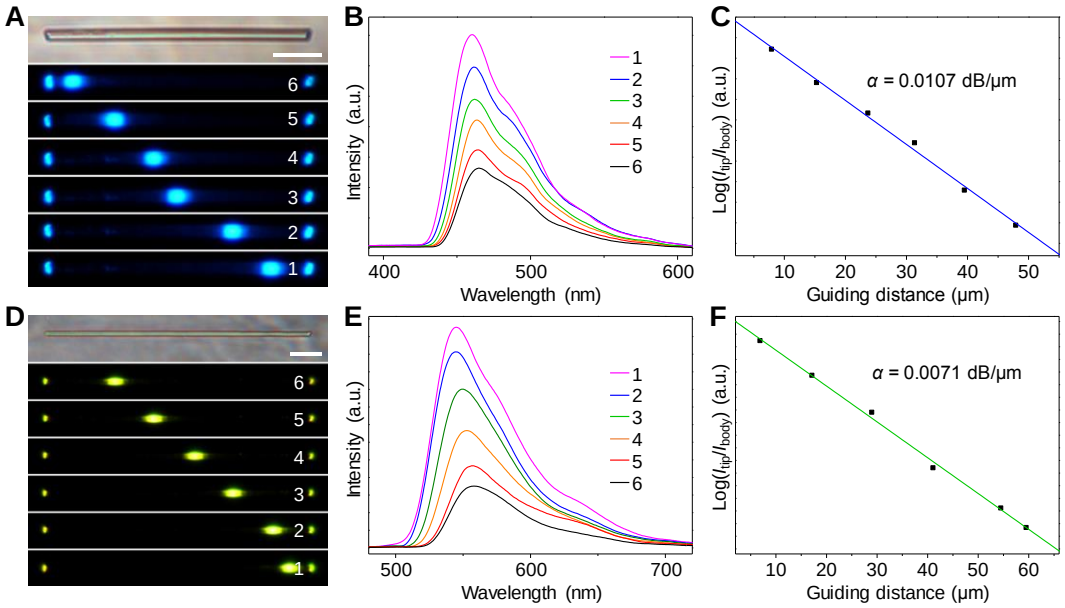

fig. S6. Optical waveguiding properties of OPV-A and OPV-B NWs. (**A**, **D**) Bright-field and PL images obtained from a single OPV-A and OPV-B nanowire by exciting the wire at different positions, respectively. Scale bars are 10 μm. (**B**, **E**) Spatially resolved PL spectra from the tips of the nanowires for different separation distances between the excitation spot and the wire tip shown in (A, D). (**C**, **F**) The logarithmic plot of relative intensity I_{WG}/I_{Ex} against guiding distance between the excited spot and the emitting tip of OPV-A and OPV-B NWs, respectively.

Spatially resolved PL imaging and spectroscopy measurements were performed by locally exciting a single wire with a 405 nm focused laser beam. The PL intensity at excitation site (I_{Ex}) and waveguiding spot (I_{WG}) was recorded when we moved the laser excitation site to increase PL guiding distance (X), as shown in fig. S6A and D. Typically, the PL intensity at the waveguiding spot gradually decreases with the increase of the PL guiding distance (fig. S6B and E). Figure S6C and F display the logarithmic plots of the relative intensity between excitation site and waveguiding spot, $\log(I_{WG}/I_{Ex})$,

against guiding distance. The curves were fitted by a function $\log(I_{WG}/I_{Ex}) = -\alpha X$, where α is the optical propagation loss coefficient (*56*). The optical propagation loss coefficients of the OPV-A and OPV-B nanowires are as low as 0.0107 and 0.0071 dB/μm, respectively, which would contribute to the realization of low-threshold lasing oscillation.

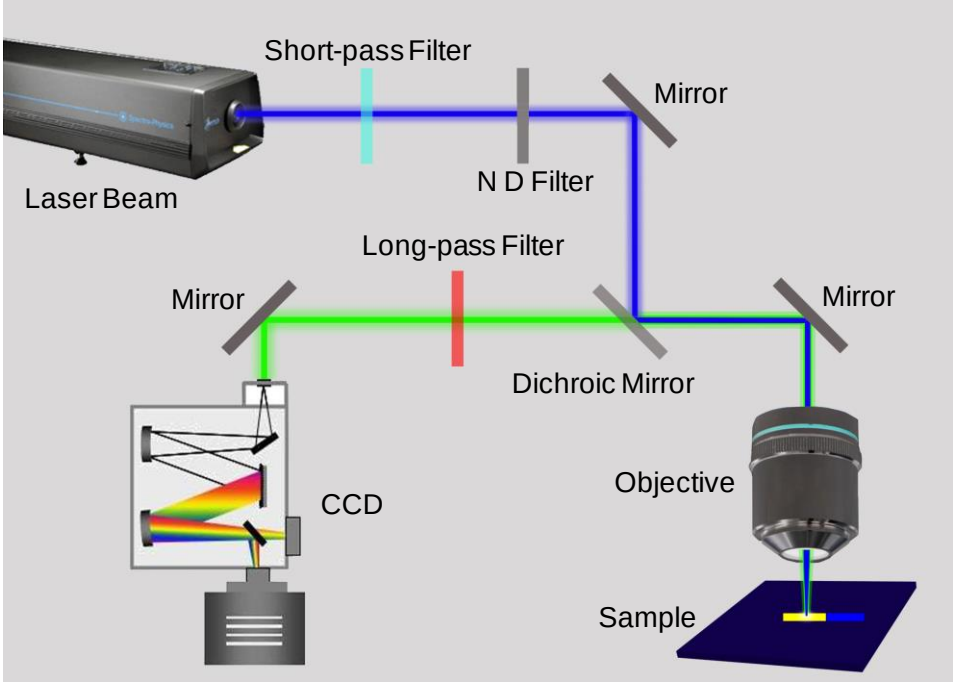

fig. S7. Schematic illustration of the homebuilt setup for optical characterization.

A homemade micro-photoluminescence (μ-PL) system was used to examine the optical properties of the NWs. The excitation pulses (400 nm) were generated from the second harmonic of the fundamental output of a regenerative amplifier (Spectra Physics, 800 nm, 100 fs, 1 kHz), which was in turn seeded by a mode-locked Ti:sapphire laser (Mai Tai, Spectra Physics, 800 nm, 100 fs, 80 MHz). The excitation laser was filtered using a 720-nm short-pass filter and then was focused down to a 40-μm diameter spot through an objective (Nikon CFLU Plan, 50×, N.A = 0.8). The power at the input was altered by the neutral density filters. The emissions from the NWs were recorded using a thermal-electrically cooled CCD (Princeton Instruments, ProEm: 1600B).

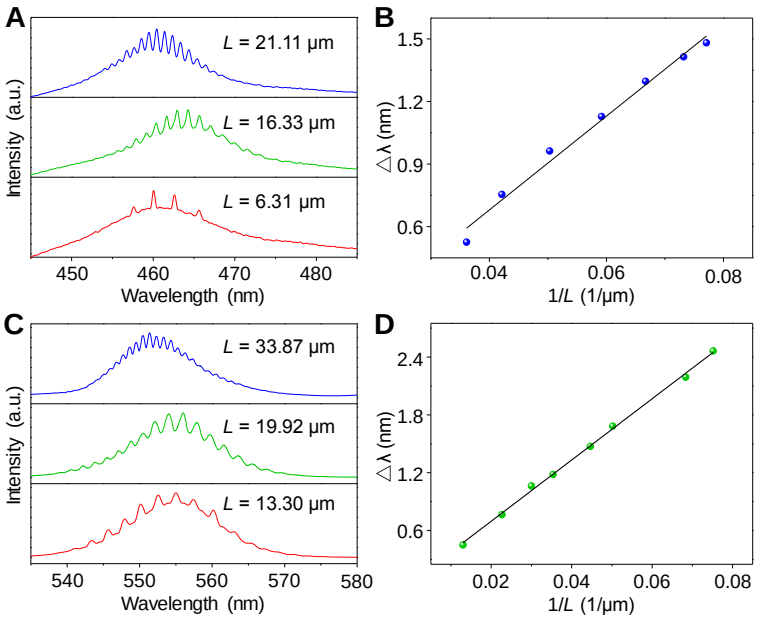

fig. S8. Microcavity effects of uncoupled NWs. (**A**, **C**) Modulated PL spectra of the OPV-A and OPV-B NWs with different lengths. (**B**, **D**) The mode spacing (Δλ) versus the reciprocal length (1/*L*) of the OPV-A and OPV-B NW, respectively, showing a clearly linear relationship.

The modulated PL spectra of uncoupled OPV-A and OPV-B NWs with different lengths were measured to study the microcavity effects. For Fabry–Pérot (FP)-type resonance, the mode spacing is given by the equation $\Delta\lambda = \lambda^2/2Ln_g$, where L is the length of the NW resonator, λ is the light wavelength, and n_g is the group refractive index. Fig. S8B and D plot the mode spacing $\Delta\lambda$ against the reciprocal length (1/L) of the OPV-A and OPV-B NW, respectively. The linear relationship indicates that the PL modulation is due to FP-type cavity resonance.

section S3. Construction of the axially coupled heterogeneous NW resonators with effective mode modulation

The controllable fabrication process of the axially heterogeneous coupled nanowire cavities is shown in fig. S9 and S10. The influence of the gap width on the mode modulation was theoretically analyzed to provide guidance for construction of the coupled NWs (fig. S11 and S12). The axially coupled heterogeneous NWs with desired gap distances were constructed by alternately exerting a lateral force to the end of one NW in the micromanipulation process, as illustrated in fig. S13. Effective optical coupling between the two NWs in the axial heterostructure can be observed (fig. S14). Figure S15 presents the pump power-dependent lasing spectra of the OPV-A and OPV-B NWs with and without the coupling of the other distinct NWs. The influences of the structural parameters, including nanowire length and gap distance, on mode modulation effect are presented experimentally in fig. S16 and S17.

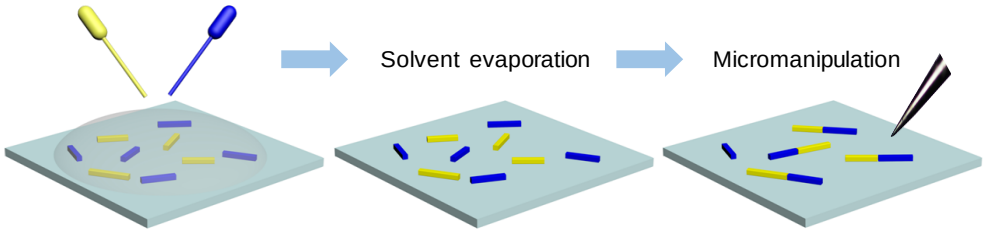

fig. S9. Schematic diagram of the fabrication process of the axially coupled heterogeneous NWs.

The axially coupled heterogeneous NW structures were prepared via a micromanipulation method. In a typical construction, the OPV-A and OPV-B NWs were first transferred onto a glass substrate by dropping and evaporating their colloidal solutions on the substrate. The NWs scattered on the substrate were then manipulated to construct the desired axially coupled heterogeneous NW resonators by using a microprobe under an optical microscope equipped with super-long working distance objective. The NWs were cut to the desired length using a bend-to-fracture method when necessary.

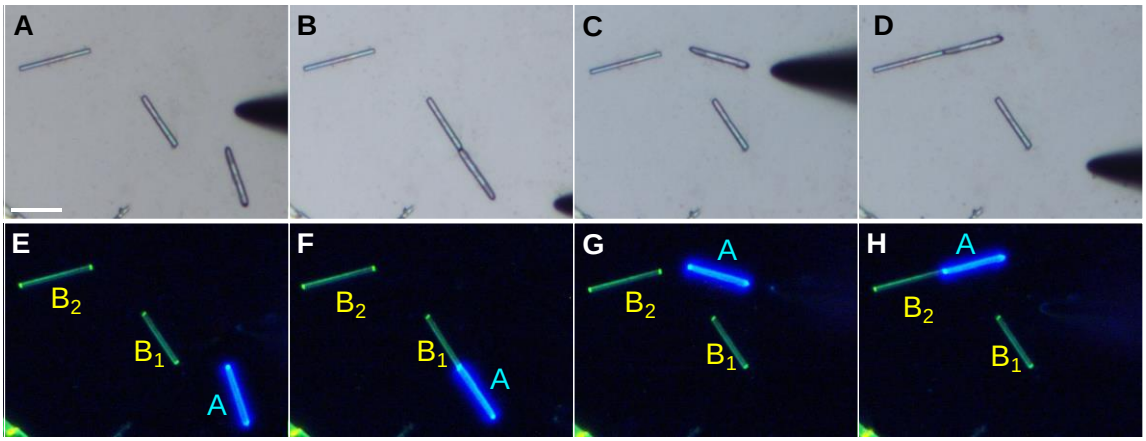

fig. S10. Controllable fabrication of the axially coupled heterogeneous NW cavities. (**A**-**D**) and (**E**-**F**) Bright-field microscopy and PL images of the NWs at different preparation stages. The black shadow in the images is the tungsten probes for manipulation. Scale bar is 10 μm.

The micromanipulation was carried out using a tungsten probe mounted on a precisely controlled three-dimensional moving stage under an optical microscope equipped with a super-long working distance objective. Bright-field microscopy and PL images show the fabrication process of the axially coupled heterogeneous NW cavities, with a certain NW, A, being controllably coupled to different NWs, B_1 and B_2. Throughout the entire preparation process, the NWs maintained the active optical waveguide property without an evident scattering point along the NW body. The as-prepared axially coupled heterogeneous NW cavities were used for the subsequent characterizations.

Effective intercavity gap distance for lasing mode modulation.

The intercavity gap distance has a great influence on the mode modulation in the coupled cavity system from two aspects as follows: (1) the optical coupling between two NWs decreases as the gap broadens; (2) the variation of the gap width leads to different phases for the light directly reflected from the end facet of the active NW and for the light reflected from the passive NW.

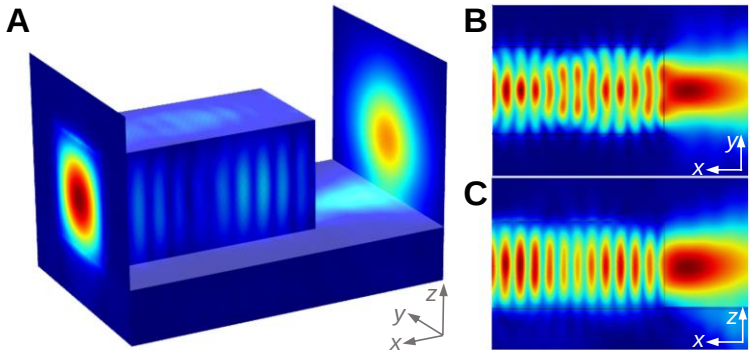

fig. S11. Three-dimensional numerical simulation of the output field from the NW end facet. (**A**) Three-dimensional numerical simulation of the output field from the NW end facet. Top view (**B**) and side view (**C**) of the field distribution. With the NW width and height both being 1 μm, the refractive indexes of the organic NW, silica substrate and surrounding by vacuum are 1.7, 1.45 and 1, respectively. The input field is the fundamental mode at 560 nm.

To provide guidance for construction of the coupled NWs, we theoretically analyzed the influence of gap width on the mode modulation. The output field from the NW end facet was calculated by using three-dimensional finite-element methods, as shown in fig. S11. The calculated transmitted field at the NW end facet decays with the propagation length because of light diffraction and energy leakage to the substrate. From the numerically

simulated results, we estimated the electromagnetic field decay length (L_d) to be 700 nm, i.e., $I_z = I_0\exp(-z/L_d)$, where I_z is the optical intensity at the distance z from the NW end face. This result indicates that the efficient optical coupling between two NWs can be achieved with the gap distance less than L_d.

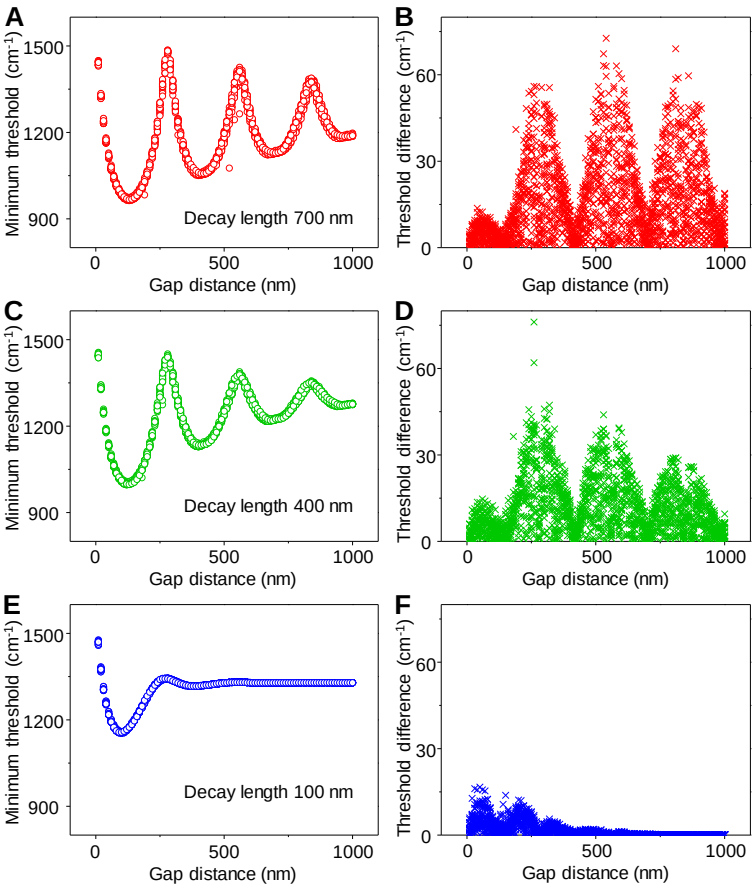

fig. S12. Influence of gap distance on the mode modulation. (**A**, **C**, **E**) Numerically simulated result of the gap distance-dependent minimum threshold of the lasing mode in the coupled NW resonators with different field decay lengths. (**B**, **D**, **F**) Difference between two lowest thresholds of lasing modes for different field decay lengths.

A more rigorous analysis was performed by calculating threshold gains of optical modes in coupled NWs with an active NW length (L_1) of 10 μm, passive NW length (L_2) of

about 12 μm, and spectral region of 540 – 580 nm. Figure S10A, C and E show the gap distance-dependent minimum thresholds for different optical field decay lengths. The threshold gain oscillates with gap distance due to the interference of light in the gap. The period of the threshold oscillation is approximately half of the wavelength. Moreover, the threshold oscillation decays with increasing gap distance and the decay rate slows down with increasing optical field decay length.

The mode selection effect is determined by the modulation of thresholds for modes in the gain bandwidth. Accordingly, we calculated the difference between two minimum thresholds of lasing modes to quantitatively illustrate the mode selection effect. As shown in fig. S12B, the phase of light in the gap plays a very important role in the mode selection, which enhances the threshold modulation when the gap distance is integer times the half-wavelength. For the optical field decay length of 100 nm, the modulation becomes smaller than 5 cm^{-1} when the gap distance is larger than 300 nm, which corresponds to the case in which the NW cross sections are comparable to the lasing wavelength (*8*). By contrast, for an optical field decay length of 700 nm, the modulation is always larger than 10 cm^{-1} over the gap range of 0 – 1000 nm. These results indicate that the mode selection effect can be obtained more easily in our coupled NW system due to the much smaller optical loss in the gap. In general, the mode selection effect in our coupled NW system has a much lower requirement on the gap distance.

In practical coupled NWs, the structure imperfections would introduce further scattering loss at the end face or higher propagation loss due to the misalignment of two component NWs. Therefore, the gap distance between coupled NWs was controlled within the range

of ~0 – 400 nm in our experiments to ensure effective optical coupling and high threshold modulation.

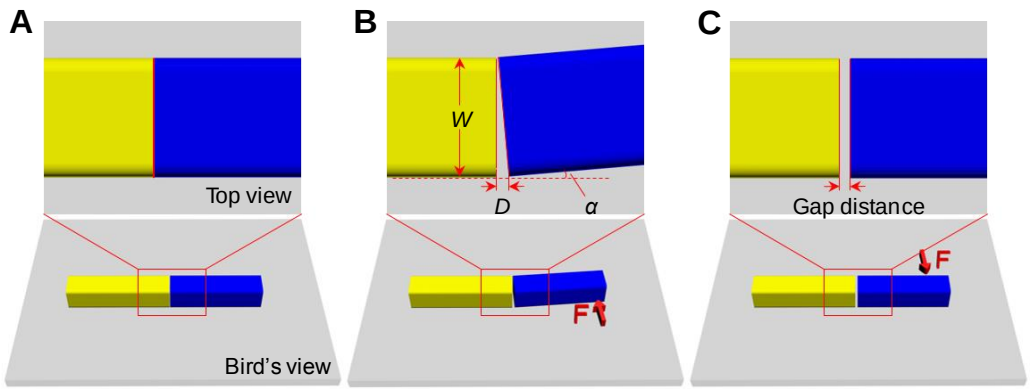

fig. S13. Schematic diagram of the construction strategy of the desired gap distance for axially coupled heterogeneous NW resonators.

We constructed the axially coupled heterogeneous NWs with desired gap distances by alternately exerting a lateral force to the end of one NW in the micromanipulation process, as illustrated in fig. S13. First, we push two heterogeneous NWs together by using a microprobe to fabricate the axially coupled structures with no/little space between two component NWs (fig. S13A). Next, one of the NWs was pushed away from the axial direction to a certain angle (α) by exerting a force to the end of the NW (fig. S13B). This force would lead to a space between the two NWs with the maximum distance $D = 2W \sin(\alpha/2)$, where W represents the NW width. Finally, the NW was move backwards by a force in the opposite direction, which would result in a gap with a distance of D (fig. S13C). This lateral force technique enables us to control the gap distance to within the range of effective coupling distances through controlling the deflected angle (α).

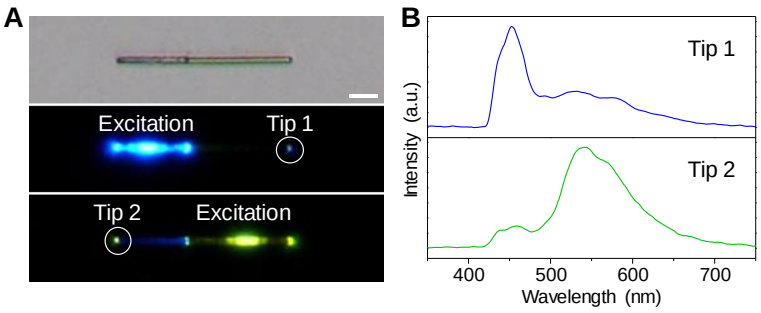

fig. S14. Coupling effect of axially coupled heterogeneous NW cavities. (**A**) Bright-field microscopy (top) and PL images of the axially coupled heterogeneous NW cavities locally excited at the OPV-A (middle) and OPV-B (bottom) NWs. Scale bar is 5 μm. (**B**) Spatially resolved PL spectra collected at tip 1 and tip 2, as marked in (A).

Fig. S14 displays the bright-field microscopy image of the as-fabricated axially coupled distinct NWs and the corresponding PL photographs locally excited at the OPV-A and OPV-B NWs. As shown in the PL images, the light emitted in the NWs can be effectively coupled between them and out-coupled from the end facets. This is further proven by the spectral characterization in which the emission from one NW is detected from the tip of the other unexcited NW. The effective optical coupling between the NWs is the prerequisite for the mode modulation in the coupled system.

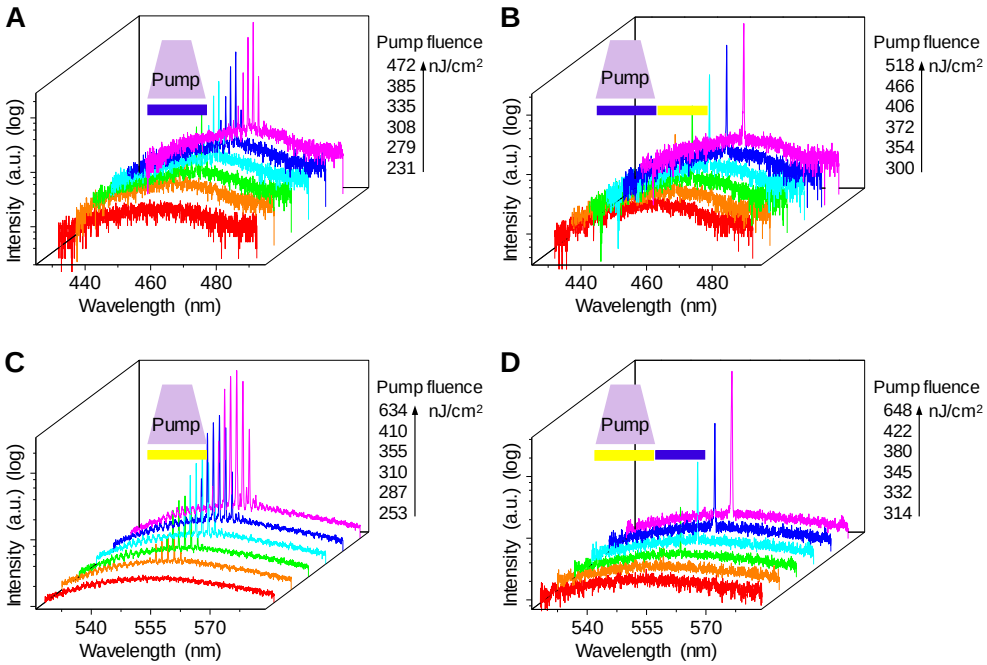

fig. S15. Evolution of the emission spectra with the increase of pump power for isolated and heterogeneously coupled NWs. (**A**, **C**) PL spectra of the isolated OPV-A and OPV-B NWs at different pump fluences. (**B**, **D**) Pump power-dependent PL spectra of the corresponding OPV-A and OPV-B NWs coupled with each other.

As shown in fig. S15A and C, both the single OPV-A and OPV-B NWs exhibit multimode lasing, resulting from inhomogeneous gain saturation caused by spatial hole burning or cavity inhomogeneity. In sharp contrast, single-mode lasing actions were realized in the OPV-A and OPV-B NWs when they were axially coupled with the other OPV-B and OPV-A NWs, respectively (fig. S15B and D). The single-mode in the heterogeneously coupled NWs operated stably over a large range of pump intensities. The pump power-dependent PL intensities are plotted in Fig. 3E and F in the main text, from which we derived the corresponding lasing thresholds. No obvious increase of the lasing threshold was observed from the OPV-A or the OPV-B NWs in the coupled NW

structures. This robust mode-selection effect cannot be achieved in single FP-type NW cavities, for which the single-mode operation is accompanied by a sharp increase of the threshold gain.

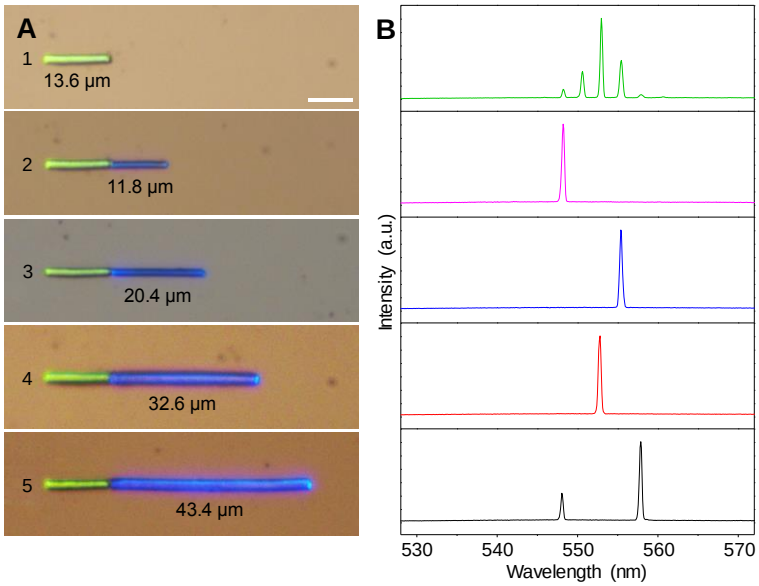

fig. S16. Lasing characterization of the OPV-B NW coupled with OPV-A NWs of different lengths. (**A**) Optical images of isolated OPV-B nanowire and the same OPV-B nanowire coupled with OPV-A nanowires of different lengths under the simultaneous illumination of a halogen lamp and a mercury lamp. Scale bar is 10 μm. (**B**) Corresponding lasing spectra of the OPV-B nanowire under different conditions shown in (A).

In the heterogeneously coupled nanowire system, the active nanowire determines the mode frequencies, while the passive nanowire causes the mode selection effect. Therefore, the length of individual nanowire has a great influence on the output mode of the coupled nanowire lasers. To demonstrate the influence of nanowire length on the mode modulation effect, we investigated the lasing properties of the same OPV-B nanowire coupled with OPV-A nanowires of different lengths. An OPV-B nanowire of 13.6 μm in length was selected as lasing cavity, while four OPV-A nanowires with different lengths of 11.8, 20.4, 32.6 and 43.4 μm as filter cavities (fig. S16A). The gaps

of these heterogeneously coupled nanowires were all controlled within the range of ~0 − 400 nm to obtain effective optical coupling. As shown in lasing spectra in fig. S16B, clear mode selection effect can be observed from all these coupled structures. When coupled with a relatively shorter OPV-A nanowire, the OPV-B nanowire output single-mode laser. The selected mode from the OPV-B nanowire varied due to the difference in threshold modulation provided by distinct OPV-A nanowires. When a longer OPV-A nanowire was applied as filter cavity, more than one modes were selected from the OPV-B nanowire. This is because the longer OPV-A nanowire supports more resonance modes, which leads to the simultaneous match of multiple modes between the lasing and filter cavities. Therefore, the nanowires with length in the range of ~10 − 25 μm were suggested for the realization of single-mode laser because they not only avoid the multimode selection but also provide sufficient optical gain.

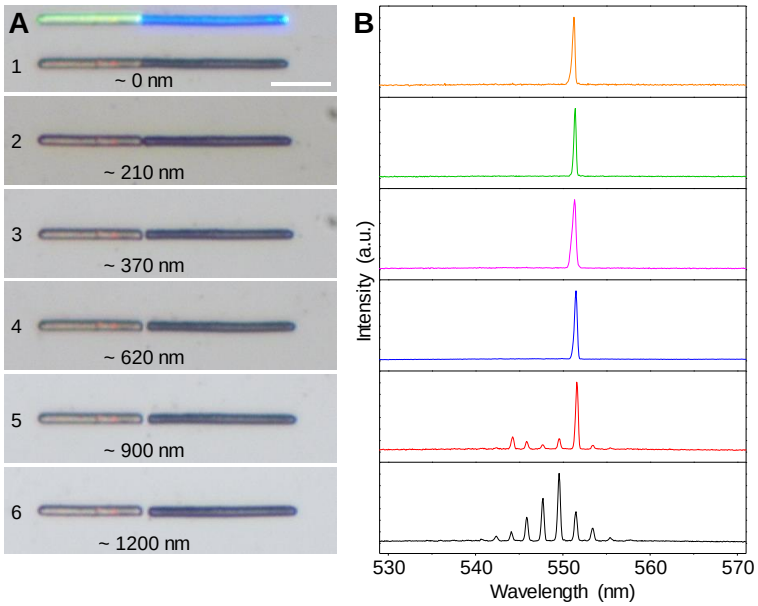

fig. S17. Lasing characterization of the axially coupled heterogeneous NWs with varying gap distances. (**A**) Optical images of the heterogeneously coupled nanowires with increasing gap distance. Scale bar is 10 μm. (**B**) Corresponding lasing spectra of the OPV-B nanowire under different conditions shown in (A).

The gap distance has a significant influence on optical coupling and thus mode modulation in coupled cavity system. To demonstrate the influence of gap distance on mode modulation, we studied the evolution of the laser spectrum by gradually changing the gap distance of the heterogeneous coupled nanowires. An OPV-B nanowire with length of 17.2 μm was selected as the lasing cavity, while an OPV-A nanowire 24.8 μm in length as the mode filter. As shown in fig. S17, the significant mode selection effect can be achieved in a large range of gap distance, ~ 0 − 600 nm. When the gap width reaches ~ 900 nm, more modes began to emerge because of the decrease of optical coupling between two nanowires. With further increase of the gap distance over 1200 nm, there is no obvious mode selection effect any more. These results confirm that the

mode selection effect in our coupled NW system has a relatively lower requirement on the gap distance, which is in agreement with the theoretical results (see fig. S12).

section S4. Numerical simulation of the effective refractivity and threshold gain

Modeling of the axially coupled heterogeneous NW resonators.

A single NW can be treated as a FP-type cavity, with the end facets serving as reflecting mirrors, as depicted in fig. S18A. For the light input from the end facets of the NW, the steady-state field distribution satisfies the following equations

$$E_2 = r' e^{-i2\beta L} E_1 \quad \text{(S1)}$$

$$E_r = rE_i + tE_2 \quad \text{(S2)}$$

$$E_1 = tE_i - rE_2 \quad \text{(S3)}$$

where E is the electric amplitude (subscripts i and r denote the incident and reflected light, respectively), L is the cavity length, r and r' are the Fresnel reflection coefficients of the left and right mirrors for light input from left-side, respectively, $t = (1 - |r|^2)^{1/2}$ represents the transmittance of the left mirror, and $\beta = nk_0 + ig$ represents the wave vector of light propagating in the NW (vacuum wave vector $k_0 = 2\pi/\lambda_0$; the imaginary part of refractive index, ig, corresponds to the gain for $g > 0$ or loss for $g < 0$). The electric intensity of the total reflection from the cavity is

$$E_r = r_c E_i \quad \text{(S4)}$$

with the cavity reflection coefficient $r_c = F_c(r, r', \beta, L)$ solved by the function

$$F_c(r, r', \beta, L) = r + r' t^2 e^{-i2\beta L}/(1 + rr' e^{-i2\beta L}) \quad \text{(S5)}$$

For the coupled NWs (fig. S18B), the end facet coupled with the filter NW can be treated as a combination of three interfaces. The effective reflection coefficient of this end facet can be solved by the function

$$r_{eff} = F_c(-r_1, r_c^{(2)}, \beta_{gap}, L_{gap}) \quad \text{(S6)}$$

with the reflection coefficient from the right NW cavity as

$$r_c^{(2)} = F_c(r_2, -r_2, \beta_2, L_2) \quad \text{(S7)}$$

where β_{gap} and L_{gap} are the parameters for the air gap between two NWs.

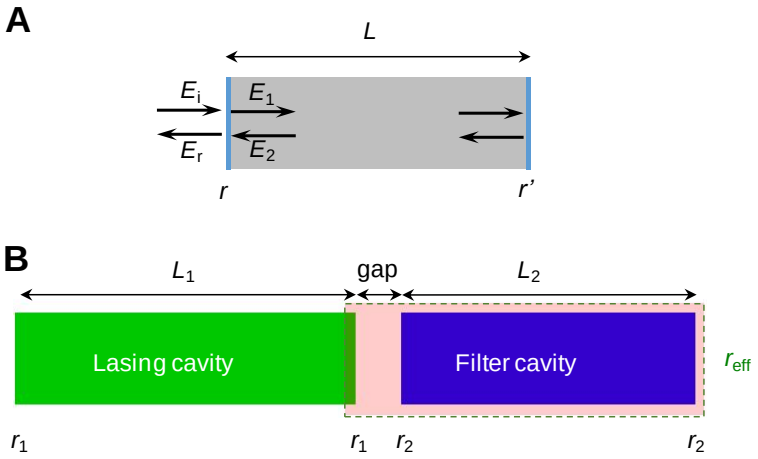

fig. S18. Theory model. Schematic illustration of (**A**) single NW and (**B**) coupled NW model, annotated with elements used in the numerical simulation.

Calculation of the effective end-facet reflectivity.

According to the previously reported works (*57,58*), the reflectivity at the end facet saturates and approaches the Fresnel equation when $nw/\lambda \geq 1$, where n is the refractive index of the NW, and w is the cross-section size of the NW. In our work, the Fresnel equation can be well applied to the calculation of the NW end-facet reflectivity as $nw/\lambda > 2.8$, with n = ~1.7, w = ~1 μm, and λ < 600 nm. Therefore, the end-facet reflectivity of single NWs can be approximately solved by $\rho = |r|^2 = (n-1)^2/(n+1)^2 \approx 0.07$. In the axially coupled heterogeneous NW cavity system, the effective reflectivity of the lasing NW at the end facet, coupled with the filter NW, was calculated with L_1 = 10 μm, L_2 = 12 μm, L_{gap} = 275 nm, $r_1 = r_2 = -(0.07)^{1/2}$, $\beta_{gap} = k_0$, and $\beta_2 = k_0 n(\lambda)$. The wavelength-dependent refractive index $n(\lambda) = n_0 - (\lambda - 550\ \text{nm})\, dn/d\lambda$. From the experimental data from fig. S8, we estimate the dispersion $dn/d\lambda = -0.005\ \text{nm}^{-1}$. The obtained calculation results are plotted in Fig. 4B of the main text.

The effective end-facet reflectivity (ρ_{eff}) of the lasing NW in the heterogeneously coupled cavities varies periodically with the wavelength. The wavelength-dependent end-facet reflectivity results in the mode modulation because the cavity modes with larger effective reflectivities are selectively amplified.

Calculation of the mode threshold gain.

A more rigorous analysis can be performed through calculating the threshold gain of the cavity modes in the axially coupled heterogeneous NW laser. The threshold gain was calculated using the coupled NW model for L_1 = 10 μm, L_2 = 12 μm, L_{gap} = 275 nm, $\beta_1 = n(\lambda)k_0 + ig$, with g being the gain of the left NW. The reflectivity from the left cavity can be solved as

$$r_c^{(1)} = F_c(r_1, r_{eff}, \beta_1, L_1) \quad \text{(S8)}$$

The optical propagation loss in the passive cavity was considered by including a small imaginary part of $-0.002i$, in the refractive index $n(\lambda)$. The diffraction effect in the gap is approximated by including a propagation loss corresponding to a propagation distance of 700 nm, which gives a imaginary part in β_{gap} as $-i/1.4$ μm. The threshold gain in the coupled NWs was obtained for $|r_c^{(1)}| = \infty$, which is plotted in Fig. 4C in the main text. The threshold gain in the single NW was calculated as a reference by using the same formula, but $r_{eff} = r_1$.

The calculated modes have nearly equal threshold gain in the isolated NW laser, which leads to multimode lasing output. For the coupled cavity structure, the threshold gain was modulated among different lasing modes, resulting from the wavelength-dependent end-facet reflectivity. With a large modulation depth of the threshold gain, the axially coupled heterogeneous NW cavity structure supports a remarkable mode selection effect.